10. ROUTINE CALIBRATION AND PAYLOAD EVOLUTION

Continuous monitoring of the geometric and photometric performances of the payload was necessary throughout the mission. This was conducted partly at ESOC (in particular for the photometric aspects), and partly by the FAST Consortium as part of their 'first-look analysis' (in particular for the geometric aspects). The focus monitoring resulted in semi-regular focus adjustments to take account of progressive evolution of the payload structure, the results of which are described in detail, and which led to a comprehensive model of moisture release and optical degradation accounting for the observed focus evolution with time. The radiation darkening of the optics, especially of the star mapper relay optics, led to an evolution of the photometric performances, which had to be accounted for in the observation time allocation, as well as during the rigorous photometric calibration as part of the data reductions.

10.1. Routine Monitoring Activities at ESOC

Payload Monitoring

A subset of the software developed for calibration purposes was adapted and built into a separate payload monitoring program for use in near real-time. The selected stars were processed to estimate their intensities and modulation coefficients. The estimated values were compared with the expected values based on the photometric parameters defining the star (brightness and colour) and based on the calibrated response of the telescope and detectors. Reports were generated for each processed observation.

The software for this task ran on the Hipparcos dedicated computer system continuously throughout the mission. It performed many tasks associated with verifying the correct performance of the on-board science data collection and processing. Every 60 s, the program selected one star observed in the preceding 30 s. The selection criteria were based on the following: (i) stars present for less than a complete observation frame of 2.133... s were not used; (ii) multiple stars and minor planets were not used; (iii) large-amplitude variable stars were preferentially selected (in order to maintain up-to-date ephemerides for them); (iv) photometric secondary standard and constant stars were preferred over non-photometric stars; (v) brighter stars were preferred over faint

stars; (vi) if the previous star to be processed was observed in the following field of view, preference for the next observation was given to stars observed in the preceding field of view, and vice versa.

This last constraint was important for quick and reliable verification of the attitude control system (see below). One star was selected, out of those possible, in a pseudo-random manner where the probability of selection was weighted according to the above criteria. The largest weighting was given to large-amplitude variable stars, so they were almost always processed, if observed.

Regardless of star type, analysis proceeded as follows. The raw image dissector tube samples were extracted from the scientific telemetry, and the rotational (body) rates of the spacecraft were extracted from the attitude control system telemetry. The raw image dissector tube samples were then decompressed and corrected for detector saturation effects according to pre-defined decompression tables. The resulting data resulted in a modulated signal $I(t)$ of the form given in Equation 1.1. The five unknown parameters $I_0, M_1, M_2, \theta_1, \theta_2$ were estimated from a Fourier analysis of the signal. Except for the stars flagged *a priori* as variable, a check of the measurement quality was made. This was done by comparing the values of I_0 and M_1 against their expected values.

I_0 quality 0, 1, 2, 3 meant that the ratio of measured to expected I_0 corresponded to a magnitude difference of less than 1, 2, 3, or 4 respectively for $B < 10$ mag; or less than 2, 3, 4, or 4 respectively for $B > 10$ mag. M_1 quality 0, 1, 2 meant that the ratio of measured to expected M_1 lay in the range 0.8–1.2, 0.6–1.4, or 0.4–1.6 respectively for $B < 10$ mag; or in the range 0.6–1.4, 0.4–1.6, or 0.2–1.8 respectively for $B > 10$ mag; The I_0 and M_1 quality flags were summed to give the overall quality flag (setting an upper limit of 3), and the results were monitored in real-time by the spacecraft analysts but were also filed for later retrieval.

The quality flag information was used to determine if the on-board real-time attitude determination system was controlling the attitude adequately. If the attitude began to drift, this would affect the ability of the on-board software to pilot the image dissector tube to the correct portion of the grid. Consequently, the measurements taken under conditions of poor real-time attitude usually resulted in quality 3 star measurements in one or both fields of view. Only if results from both fields of view showed consistently quality 0 measurements was real-time attitude determination considered to be operating successfully.

A further off-line task analysed the payload monitoring results on a weekly basis compiling a list throughout the mission of intervals of ‘good’, ‘bad’ or ‘unknown’ piloting. This was supplied to the data reduction consortia to assist in the routine data reduction activities. Only intervals of ‘good’ data would be processed. When starting to process an interval of data, the algorithm assumed a status of ‘unknown’ until the first payload monitoring report. Piloting status would only change to ‘good’ if three consecutive observations in both fields of view were assigned as quality 0 measurements. Piloting status would only change to ‘bad’ once three consecutive observations in one or other field of view were assigned with non-zero quality flags. This proved to be an effective set of criteria for defining when real-time attitude determination was converged and useful scientific data was being obtained.

Focus Monitoring

The monitoring of the focus evolution and offset from current to best focus was done by means of the M_1 values computed by processing a four-hour batch of image dissector tube telemetry, in a similar manner to that described in Section 5.6. Since the position of best focus was evolving continuously the refocusing calibration was performed every week throughout the mission (or more regularly in the case of anomalies). The best focus position could be calibrated by computing the average grid modulation coefficients M_1 over a four hour period of data. These M_1 averages were then converted into a focus offset and hence, via the history of grid movements, into an absolute focus position using the calibrated curves shown in Figure 5.4.

The motor which changed the focus position, did so in steps of 1.38 μm, and the intention was to keep the focus position on-board within ± 1 step of the best focus position. In December 1989, the results from the ground software appeared to imply that the best focus position was changing at an increasing rate, in contradiction with pre-launch predictions. It was subsequently found that the change of focus was not actually taking place, but rather that the stepping motor was incapable of moving by only one step at a time. This was later confirmed by the manufacturer. Subsequently, only focus moves of two or more steps were commanded without further problems or degradation of the science data.

Background Noise Monitoring

The star mapper proved to be very sensitive to the radiation environment in the van Allen belts and during periods of high solar activity. The result was blinding close to perigee. Moreover the radiation environment could change rapidly, as a result of solar flares. This had a direct impact on the altitude at which re-initialisation of the on-board real-time attitude determination could be attempted following perigee passage, since ground-based star pattern recognition required frequent star transits to be identified in the star mapper data stream.

As a result, the overall star mapper signal in both channels was constantly monitored with a report produced every minute giving an integrated average to the ESOC flight control team. Only once noise levels were at an acceptable level, were ground real-time attitude determination initialisation procedures performed (see Chapter 14).

Spacecraft Performance Evaluation System

For Hipparcos, ESOC used a software system called the ‘spacecraft performance evaluation system’ for close to real-time anomaly analysis as well as long-term history performance evaluation studies. This service software, running alongside the spacecraft control and operating system (at the time the ESA standard for spacecraft control and operations), regularly transferred housekeeping telemetry, event data and generated telecommand history, from the on-line mission dedicated computers to the off-line spacecraft performance evaluation machine, via a high speed HYPERBUS inter-computer link.

Every hour, all spacecraft data collected by the real-time systems were checked and consolidated. After checking, the data were archived automatically in the Hipparcos data base. The system also maintained a copy of the on-line spacecraft control and operating system data base, updated via regular transfers, which gave the users means to manipulate the data, similar to those provided by the on-line control system.

At this point the data was available in an automatic cartridge storage and retrieval system. The associated software provided, on an off-line basis, certain functions to retrieve and manipulate the data. These included alphanumeric printouts, data retrievals over as long a time interval as desired (up to the duration of the entire mission), different time sampling strategies, tape production, graphical representation of parameters, etc. In particular it was possible to schedule the routine daily retrievals and graphical colour printouts and have them automatically produced by the system. As an example of its performance, the last version of the spacecraft performance evaluation system was able to scan through a complete year of data in little more than one day.

In addition, the system provided an operative language and compiler, allowing the definition and use of derived parameters in an easy and interactive way (a derived parameter is the result of an algorithm which involves the use of a certain number of already existing and defined telemetry parameters). All tools were widely and intensively used to evaluate spacecraft performance, accomplish subsystems trend analysis and were key instruments in the study and assessment of spacecraft anomalies. Specifically, the system was used on a daily basis to monitor the troublesome behaviour of the gyros and the degradation of the payload heaters in the thermal control electronics.

Since the beginning of the mission, the system provided flexible access to the complete satellite telemetry. This meant that it was able to support simultaneously several missions, and several users within each mission, in parallel. Taking advantage of this design feature, direct access to the system was made available to external users at ESTEC. Industrial firms involved in the project could also use it in a remote mode for their own studies and assessments.

10.2. Payload Calibration

Basic Angle and Grid Rotation

During commissioning activities, ESOC performed one preliminary calibration of the basic angle (the angle separating the two fields of view) using the ground real-time attitude determination system (see Section 14.3). The value obtained was 58° 30 arcsec, compared to an on-ground calibrated value of 58° 42 arcsec. The grid rotation estimate proved to be rather unreliable, although the maximum error of about 3 arcmin was in any case shown in simulations not to impact on ground real-time attitude determination accuracies.

During the remainder of the mission, more accurate calibrations were performed by the FAST Consortium's 'first-look' facility at Utrecht. The evolution in the basic angle is shown in Figure 10.1, using all points from the NDAC and FAST Consortium's great-circle reductions. After initially decreasing, the basic angle began to increase, having reached a minimum value of $58° 0' 31.''240$. The overall evolution of the basic angle was

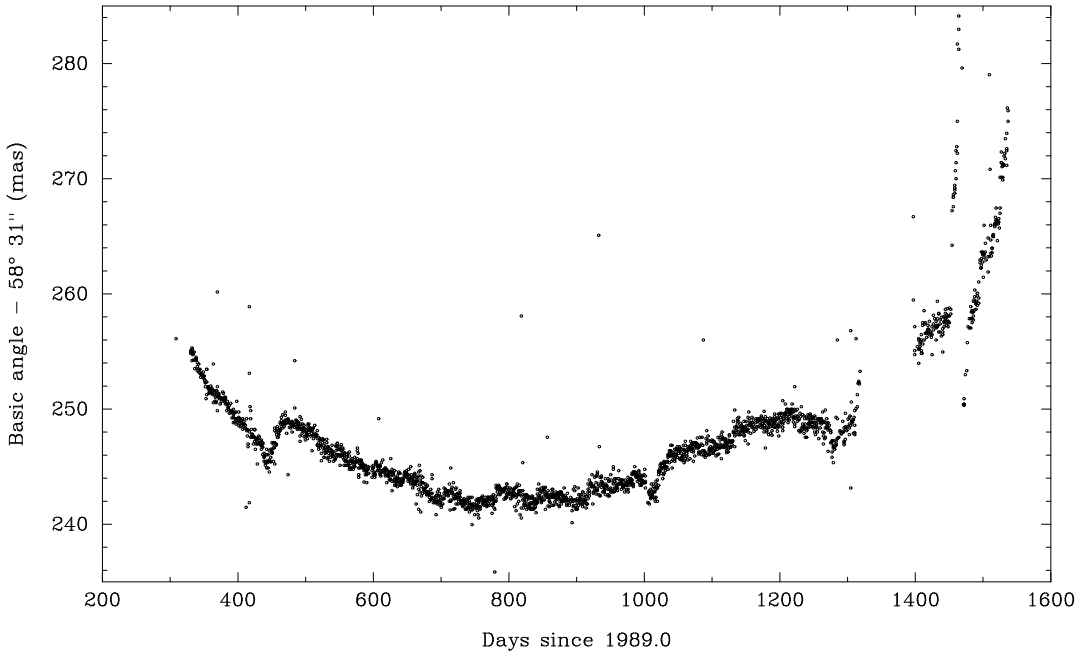

Figure 10.1. *Basic angle evolution as a function of time, determined from the preliminary great-circle reductions (see also Figures 10.12(a) and (b)). The smooth evolution with time results from contributions such as outgassing of the structure, radiation effects on the optics, and other ageing processes. Outlier points typically arise from thermal variations in the payload, described in further detail in Section 12.4. The overall evolution of the basic angle was well within specification, and well within the changes that could be modelled in the instrumental calibration on ground.*

well within the design specification, which called for a variation of below 1 milliarcsec within any 12-hour interval.

Instantaneous Field Of View Pointing

A description of the internal star pattern assembly and grid reference marks calibrations, relevant for the instantaneous field of view pointing calibration, was given in Section 5.4. The internal star pattern assembly calibration was repeated every two weeks throughout the mission. The grid reference marks calibration and coil currents calibration matrix uplink were performed daily. Typically, the standard deviation of the variation of the piloting currents was measured as 0.9 arcsec per day, i.e. the stability of both the image dissector tube pointing non-linearity, and the rigid body displacement, was very good.

Optics Darkening

Once per week, several off-line tasks were performed to analyse all data acquired by the payload monitoring software during that period. The products from the analysis included an averaging of the intensities and grid modulation coefficients contained in the image dissector tube and star mapper reports. This gave an overall evaluation of the photometric degradation of the payload due to, for example, glass darkening or

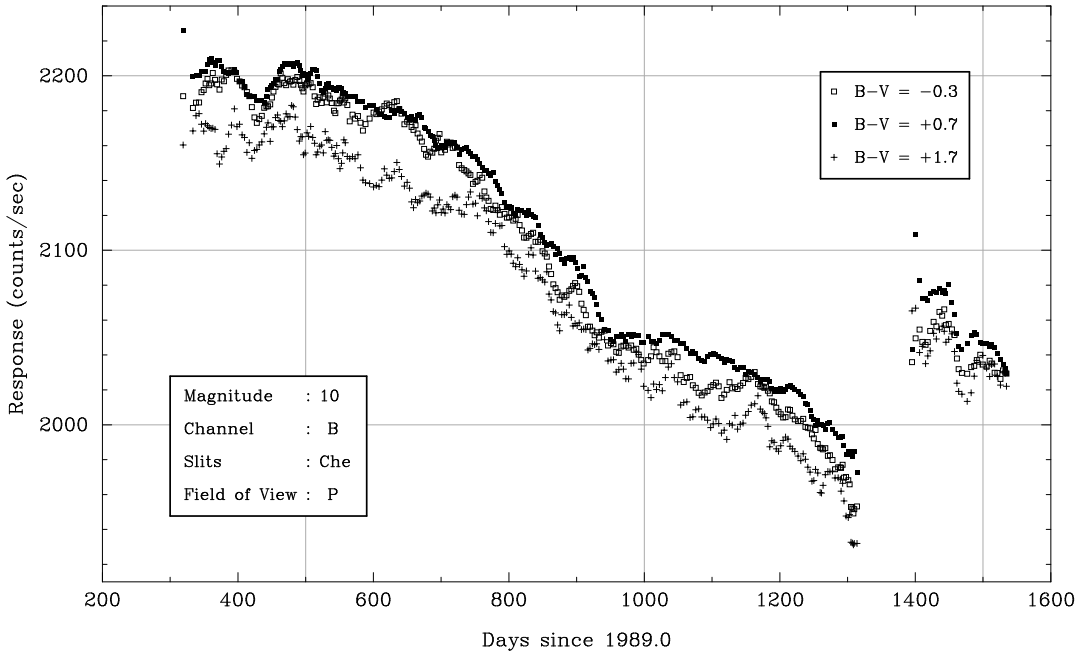

Figure 10.2. *Star mapper photometric response as a function of time, for three different ranges of star colour. The total degradation in the star mapper response throughout the mission amounted to about 10 per cent. The response improved towards the end of the mission, after the 'hibernation phase', probably because of the overall environment that the payload had been subjected to during the sun-pointing phase.*

temperature instabilities. Up to mid-February 1990 the individual star reports were processed in batches of 5000, and after that date, approximately once per week.

The results of the photometric calibrations are shown in Figure 10.2 for the star mapper response, and in Figure 10.3 for the image dissector tube response and for the first and second modulation coefficients. There was only marginal degradation throughout most of the three-gyro operations phase. However, by the beginning of 1992, the deterioration of gyro 5 began to affect real-time attitude determination accuracy which in turn affected the ground software which reduced the image dissector tube data. Further details of the evolution of the instrumental parameters are presented in Volume 3.

Other Payload Calibrations

ESOC was responsible for the initial calibration of the star mapper single-slit response profiles described in Section 5.3, the initial calibration of the instantaneous field of view profile described in Section 5.7, and for the initial chromaticity calibration activities described in Section 5.8. Subsequently, these parameters were calibrated in greater detail as part of the routine data analysis (see Volume 3).

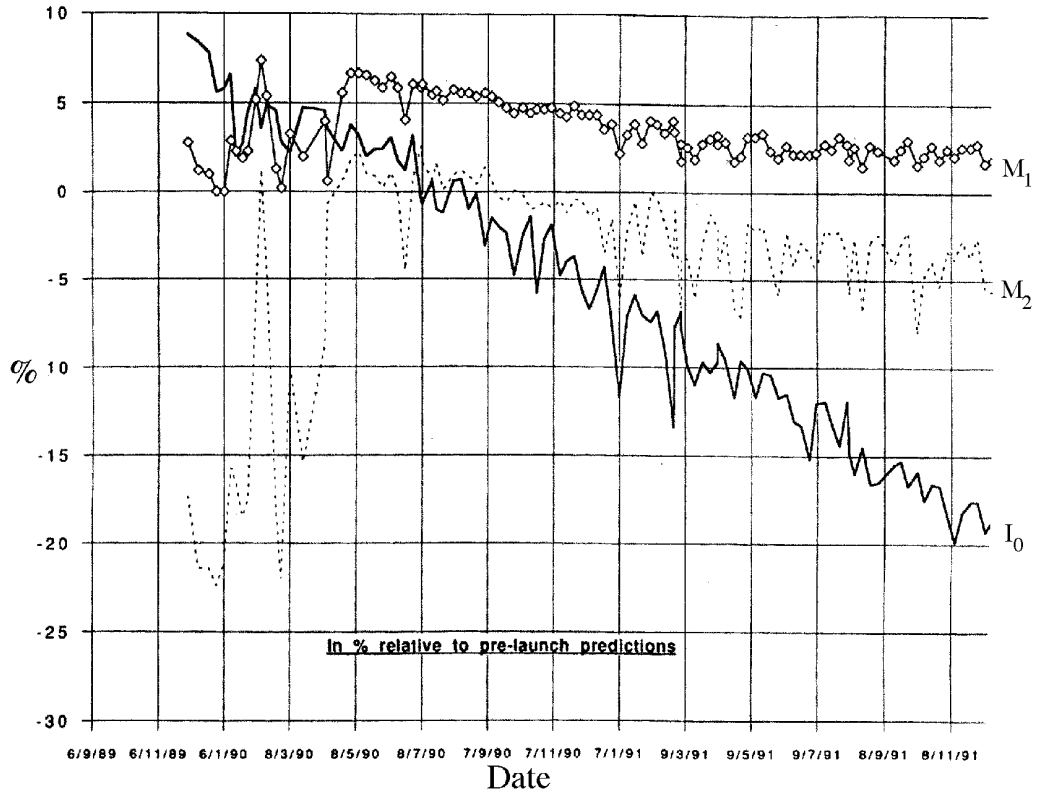

Figure 10.3. *Evolution of the image dissector tube response (I_0) and modulation coefficients (M_1 and M_2, with respect to the pre-launch predictions) with time.*

10.3. Focus Evolution

The variation of the best focus position was continuously monitored on ground through analysis of the modulation coefficients. It had been predicted that the best focus position would evolve with time due to moisture release from the carbon-fibre structure, and a focus mechanism was implemented within the payload to compensate for the expected structural evolution (to minimise the effects of a possible failure of this mechanism, it was set, pre-launch, to a position which would have given good modulation after several weeks in orbit).

In practice, significant deviations with respect to the predicted focus evolution appeared after 6 months in orbit, with the focus shift increasing more-or-less linearly from that date, and with both the amplitude and the time constant of the variation being greater than had been predicted before launch (Figure 10.4). This evolution was also accompanied by a 'differential defocus' between the best focus position of each of the two fields of view (see Figure 5.4). Consequently, the adopted focus position was taken to be the mean of the two optimum values, leading to a resulting decrease in the modulation coefficients for each of the fields of view. The details of the observed focus shift, and

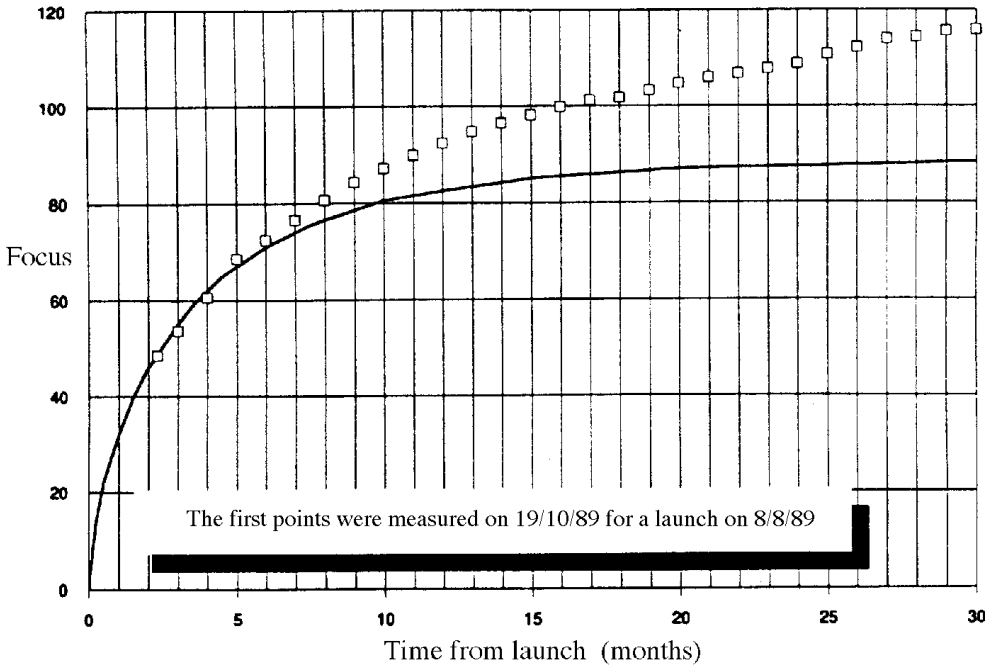

Figure 10.4. *Focus variation due to moisture release versus time. The solid line shows the pre-launch prediction of the best focus position, and the squares indicate the measured focus position.*

the conclusions of the specific study undertaken to understand the cause, are presented in detail in this section.

The theoretical behaviour of the telescope focus position was modelled prior to launch. It had been predicted to vary linearly with time, depending on the moisture content of the payload structural material. The moisture contained in the structure before launch was assumed to be homogeneously distributed, inside the material and between the payload panels, and was predicted to decrease with time as a result of 'outgassing', leading to a relationship of the form $M(t) = M_i \times G(t)$, where $M(t)$ is the moisture content at time t; M_i is the initial moisture content before the release started, and $G(t)$ is a time-dependent parameter approximated by:

$$G(t) = 1 - \exp\left[-7.3 \times \left[\frac{D \times t}{S^2}\right]^{0.75}\right] \qquad [10.1]$$

To model the evolution the following approximations were used:

$$G(t) = \frac{4}{\sqrt{\pi}} \times \frac{\sqrt{D}}{S} \times \sqrt{t} \qquad \text{for} \quad y \le y^* \qquad [10.2]$$

$$G(t) = 1 - \frac{8}{\pi^2} \exp\left[-\pi^2 \frac{D}{S^2} t\right] \qquad \text{for} \quad y \ge y^* \qquad [10.3]$$

where $y = \pi^2 Dt/S^2$ is a dimensionless function of time, $y^* = 0.52564$, $t^* = y^* S^2/(\pi^2 D)$, and D is the diffusivity of the material (in the direction normal to the surface). S is equal to the thickness k of the material when both sides are exposed to the same environment (free vacuum space in this case), and $S = 2 \times k$ when one side is obstructed (partial obstruction leading to an intermediate value).

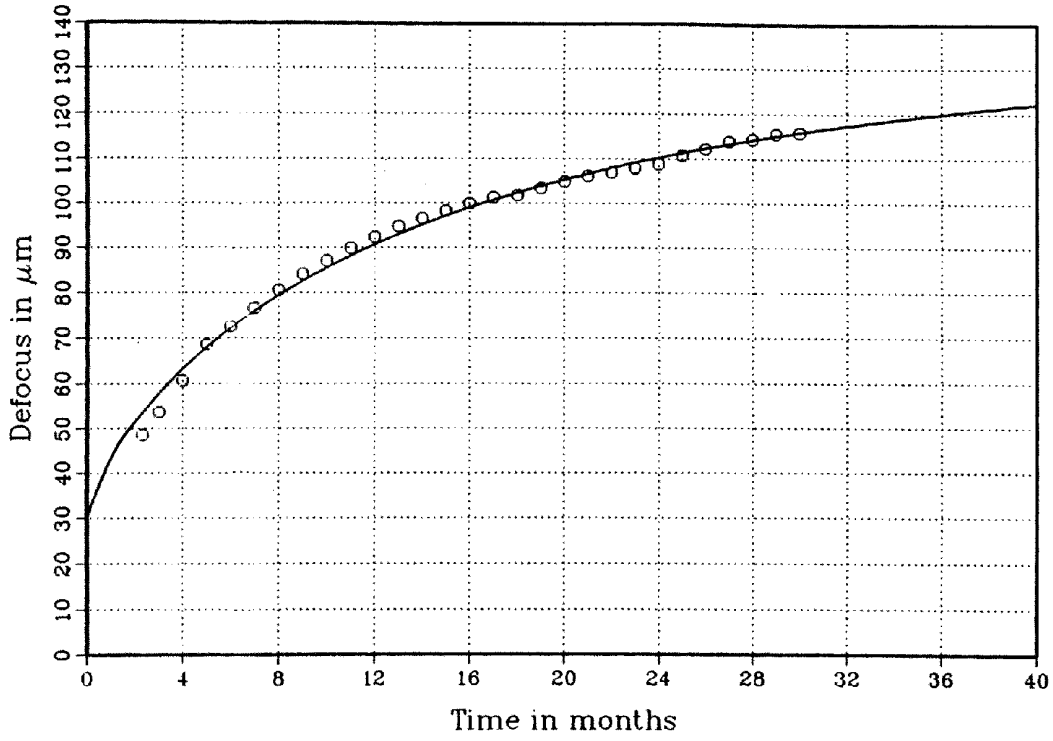

Figure 10.5. *Measured focus position and best fitting curve assuming pure moisture release according to Equation 10.6. This simple model fit to three free parameters did not provide a convincing physical explanation of the observed focus change.*

The diffusivity of the material depends on the temperature according to:

$$D = D_0 \exp\left[C\frac{T - T_0}{T \times T_0}\right] \qquad [10.4]$$

with C = 6000 K. A typical figure for carbon-fibre reinforced plastic is $D_0 = 3.8 \times 10^{-8}$ mm^2 s^{-1} at T_0 = 300 K. From the linear variation of the focus position with the moisture content, the actual focus position can be written:

$$F(t) = F_i + f_m \times G(t) \qquad [10.5]$$

where F_i is the initial focus position, and f_m is the amplitude of the variation of the focus position from the initial (moist environment) position to the final (completely dry) position, which is proportional to the final moisture content M_i. A best fit of the measured data with Equation 10.5 using for $G(t)$ the approximation given by Equation 10.1 yields:

$$F(t) = 30.3 + 104.2\ (1 - \exp(-0.134 \times t^{0.75})) \qquad [10.6]$$

where $F(t)$ is measured in microns and t in months. The plot of Equation 10.6 with the measured data indicates an apparently good fit for $t > 6$ months (Figure 10.5). However with three free parameters (F_i, f_m, and the exponent), a good fit is not necessarily consistent with the known physical properties of the system.

At the constant temperature of the telescope panels, 19 °C, the diffusivity is given by $D = 2.2 \times 10^{-8}$ mm^2 s^{-1} (from Equation 10.4), with the best fit provided by Equation 10.6 yielding a substrate thickness S = 3.42 mm. Being roughly twice the average panel thickness (1.7 mm), this result suggested that moisture release was taking place through

one side only, as if the secondary structure on the other side of the telescope panels (accommodating the heater mat carriers) was creating a hermetical sealing on the outer sides.

The most significant change of focus position occurred within about 6–8 months after launch (see Figures 10.4 and 10.5). For this interval, the approximation given by Equation 10.2 for the case $y \leq y*$ is applicable, since $t \leq t* = 324$ days on the basis of the above values of D and S. This indeed results in a rather reasonable fit, i.e. a linear dependence of the focus position with the square root of time:

$$F(t) = 5.7 + 27.7 \times \sqrt{t} \qquad [10.7]$$

as depicted in Figure 10.6(a). Equation 10.7 relates the amplitude of the variation of focus f_m to the thickness S as:

$$f_m \times \frac{4}{\sqrt{\pi}} \times \frac{\sqrt{D}}{S} = 27.7 \qquad [10.8]$$

Using the value of S deduced above, i.e. $S = 3.42$ mm, leads to $f_m = 175\ \mu$m, inconsistent with the value of f_m given by Equation 10.8, $f_m = 104\ \mu$m. On the other hand, with $S = 1.7$ mm (corresponding to moisture release through both sides) $f_m = 87\ \mu$m, very close to the pre-launch prediction of 89 μm. Figure 10.6(b) indicates that the focus evolution is well approximated by Equation 10.3 as:

$$F(t) = 5 + 90 \times \left(1 - \frac{8}{\pi^2}\right) \exp(-0.195 \times t) \qquad [10.9]$$

yielding approximately the same value for $t = 0$ ($F_i = 5\ \mu$m) as Equation 10.7, and also roughly the same amplitude of focus variation ($f_m = 90\ \mu$m). This tended to confirm the validity of the initial moisture release prediction, and suggested that conclusions drawn directly from the overall best fit to the measured data may be misleading.

The pre-launch prediction of the focus variation due to moisture release was based on the dry-out of several carbon-fibre reinforced plastic samples after thermal vacuum testing (weighed before and after the dryout sequence), and a test campaign including space conditioning at 50 °C over 5 days before the thermal vacuum test itself. A total focus variation of 38 μm was measured during the test. Samples of the carbon-fibre reinforced plastic were placed within the payload and weighed before and after the test. The prediction of the total focus variation of the telescope was obtained from $f_m \times (M_B / M_D)$ where M_B is the mass loss (before the thermal vacuum tests) of the carbon-fibre reinforced plastic samples after dry-out, and M_D is the mass loss of the samples during the thermal vacuum tests. This assumed that the amount of moisture release of the telescope structure during the thermal vacuum tests was equal to that of the samples. The time constant followed from an assessment of the diffusivity itself obtained from the measured focus variation over the space conditioning (33 μm during 5 days at 50 °C) and an assumed temperature of 20 °C during the orbital life. The resulting prediction was:

$$F(t) = 89 \times (1 - \exp(-0.427 \times t^{0.75})) \qquad [10.10]$$

with t in months. Closer analysis of the space conditioning sequence revealed an interval where the temperature was stable, and where a ‘pure’ moisture release effect presumably took place. Before and after this stable interval, thermoplastic effects due to the large temperature variations were superimposed on the moisture release effect. During this

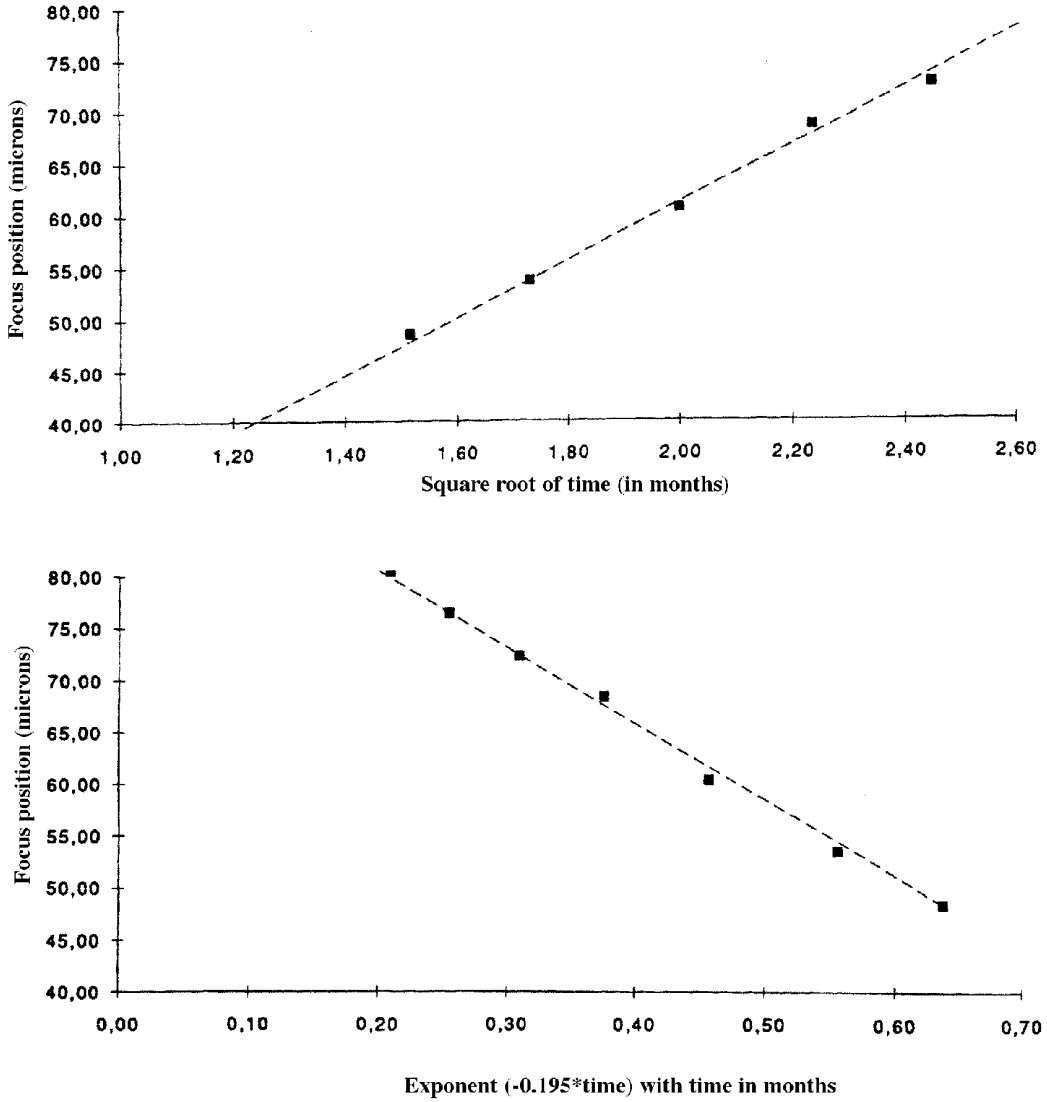

Figure 10.6. *(a) Linear approximation of the focus variation with* t^{-2} *and (b) linear approximation of the focus variation with* exp (*t*).

period, the focus position varied linearly with the square root of time as expected from Equation 10.2 such that:

$$F(t) = F_i + 2.626 \times \sqrt{F} \qquad [10.11]$$

As before, the total focus variation due to the moisture (f_m) is related to the thickness S and the diffusivity D as:

$$f_m \times \frac{4}{\sqrt{\pi}} \times \frac{\sqrt{D}}{S} = 2.626 \qquad [10.12]$$

With $D = 1.49 \times 10^{-7} \times 3600$ mm^2 hr^{-1}, at 49.5 °C, the measured temperature during the stabilised space conditioning, this gives S = 1.7 mm, f_m = 85 μm. This value was again close to the predicted one (89 μm) and also to the one obtained from the first points measured in-orbit (90 μm) assuming the same thickness S = 1.7 mm. The reassessed in-orbit 'prediction' at 19 °C was then:

$$F(t) = 89 \times (1 - \exp(-0.353 \times t^{0.75})) \qquad [10.13]$$

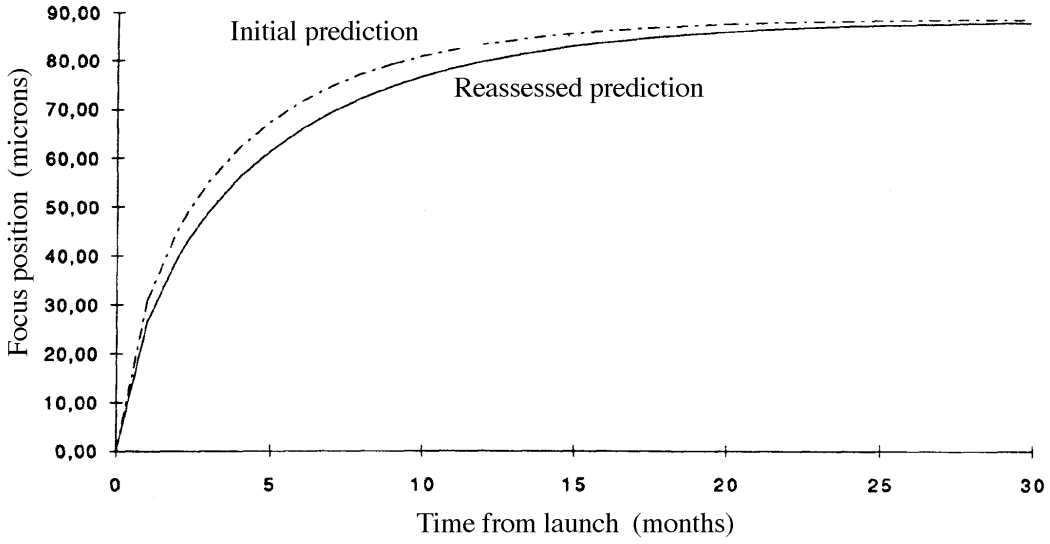

Figure 10.7. *Initial and reassessed moisture release predictions.*

very close to the initial prediction given by Equation 10.10 with, however, a slightly higher time constant (Figure 10.7).

Before turning to the origin of the discrepancy in the measured versus predicted focus evolution in-orbit, further evidence that the payload evolution had not been fully understood was given by the change in the modulation factors M_1, M_2 at the common best focus. The common best focus was adopted to be the mean of the best focus of the preceding and following fields of view. While the common best focus position had been evolving roughly according to the pre-launch predictions, the individual focus positions of the two fields of view were diverging, leading to a 'differential defocus', and a significant (and unexpected) degradation of the modulation coefficients with time (see Figure 10.3), albeit at a rate (-2.5 per cent per year for M_1) not large enough to severely impact the scientific data. The evolution of the differential defocus is shown in Figure 10.8.

Meanwhile the intrinsic optical quality of the telescope remained essentially unchanged since the beginning of the mission, as indicated by the stability of the modulation factors M_1, M_2 at the individual best focus for each field of view.

The differential defocus continuously increased with time, apparently linearly up to about 20 months after launch at a rate of $\simeq 0.66$ μm per month, thereafter remaining almost stable. This suggested a phenomenon other than moisture release was occurring, inducing deformations of the mirror surfaces, and resulting in changes of curvatures which were somewhat different for the two fields of view.

The identification of the increasing differential defocus with time suggested an average linearly varying defocus additional to the moisture release. The measured focus positions were found to be well represented by (Figure 10.9):

$$F(t) = 89 \times (1 - \exp(-0.353 \times t^{0.75})) + 0.82 \times t \qquad [10.14]$$

The additional linear variation amounted to 0.82 μm per month, corresponding to an increase of the telescope focal length. Two possibilities were considered: (a) stress release within the telescope mirrors, and (b) irradiation effects on the telescope mirrors.

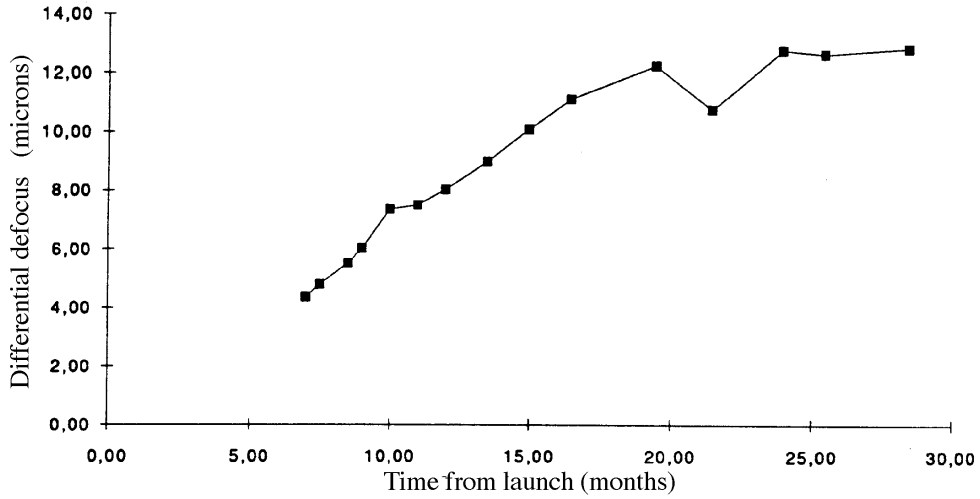

Figure 10.8. *In-orbit measured differential defocus.*

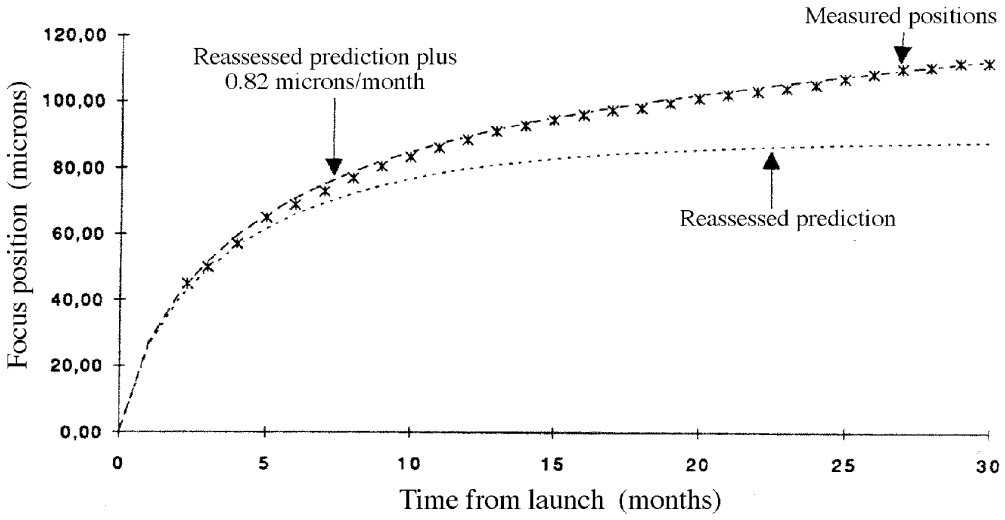

Figure 10.9. *Measured (crosses) and reassessed (lower curve) focus positions, and the reassessed focus position combined with an additional linear evolution due to optical deformation (upper curve).*

The latter was believed to be the origin of the phenomenon observed. This conclusion was based on test results obtained by bombarding samples of zerodur with very high doses (1–100 Mrads) of electrons representing 10–1000 years in low-Earth orbit (Rädlein 1991). This created a density increase of the top layers of the glass surface resulting in convex deformations of initially plane mirrors. For example, sags in the range of 1–10 μm were obtained with a zerodur disc of 100 mm diameter, and 5 mm thickness.

From Table 10.1 and Figure 10.10 it is apparent that the dose level, for 10 years in low-Earth orbit (1.3×10^4 Gy), is comparable to that observed by Hipparcos, after 2.5 years in its highly eccentric orbit, when shielded by 2.5 mm of aluminium over 4π steradians. However, the extrapolation of the sample results to the case of the Hipparcos mirrors is non-trivial. Several factors had to be considered, such as: (i) their diameter (300 mm)

Table 10.1. Dose levels.

Electron Dose 0.8MeV +0.3MeV	equivalent to time in orbit	Zerodur
20.5 Gy + 1.3×10^4 Gy	10 years	-1.6 μm
4.1×10^3 Gy + 1.3×10^6 Gy	10^3 years	-12.5 μm

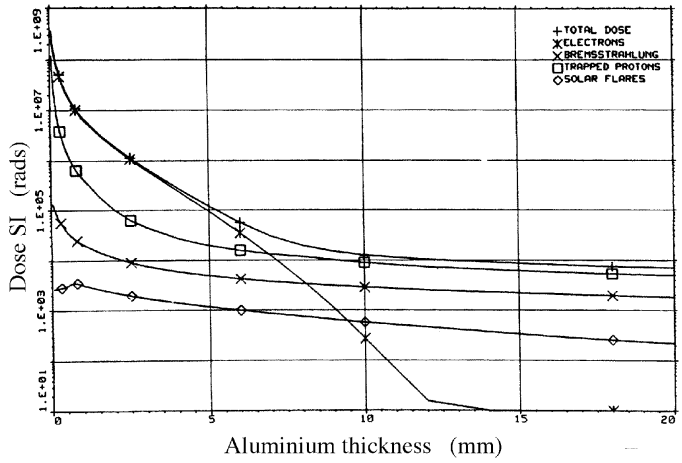

Figure 10.10. *The irradiance dose/depth curve for Hipparcos after 2.5 years in its highly eccentric orbit. The different curves indicate the effects of the different particle components*

and thickness (100 mm for the beam combiner, 60 mm for the spherical and folding mirror); (ii) the irradiation levels actually experienced by each mirror; (iii) the sensitivity to the irradiance dose (linear up to 10^5 Gy); and (iv) an understanding of the physical effects involved within the mirror substrates.

It was suspected that the spherical mirror was the most seriously affected one (on its back side), based on the sign of the additional linear variation. This acted as if the focal length of the telescope were increasing, at the rate of $\simeq$ 10 μm per year, i.e. as if the rear sides of the mirrors were more irradiated then the optical surfaces. Supporting this was the actual configuration of the payload hardware—the folding mirror was relatively well shielded, on its back side, by the focal plane assembly platform, whereas the beam combiner was least sensitive to surface deformations originating from irradiation due to its thickness. Moreover, both beam combiner and folding mirror were better shielded than the spherical mirror due to the spacecraft configuration.

Measurement of the mean scale value in the fields of view allows determination of the effective focal length in terms of the grid dimensions. This was done as part of the geometrical payload model described in Section 10.5, leading to the conclusion that the focal length did *not* change much over the mission. It would then appear that the dimensional variations of the structure, due to moisture release or some other process, continued over a much longer time than expected from the previous discussion.

Table 10.2. Photometric evolution.

Colour group	rate (per cent per day)	loss (per cent)
$-0.625 < B - V < 0.125$	−0.0343	29.94
$0.125 < B - V < 0.875$	−0.0356	31.08
$0.875 < B - V < 1.625$	−0.0313	27.39

10.4. Photometric Evolution

The photometric evolution of the image dissector tube was monitored using two independent sets of data: (i) the telemetry used for determination of the telescope focusing; and (ii) the post-processing of real-time payload monitoring results. The latter were also used to monitor the evolution of the star mapper photometry.

For off-line analysis the count rates were calculated assuming the following count rates for the three colour groups for stars of magnitude $B = 9.5$ mag:

$$-0.625 < B - V < 0.125\text{: } 1193.1 \text{ counts s}^{-1}$$
$$0.125 < B - V < 0.875\text{: } 1774.8 \text{ counts s}^{-1}$$
$$0.875 < B - V < 1.625\text{: } 3268.4 \text{ counts s}^{-1}$$

A quadratic curve for the colour dependency was assumed, and the expected value of I_0 was scaled for the magnitude dependency by:

$$10^{0.4(9.5-B)} \qquad [10.15]$$

Approximately 2.5 hours of image dissector tube data were processed, including all photometric constant and standard stars in the range $B = 1 - 9$ mag over the entire field of view. The mean weighted error in I_0 for each colour group in each field of view, $(I_0' - I_0)/I_0$, was calculated where I_0' was the measured intensity and I_0 was the predicted intensity. The final averaged results were then used to modify the three count rates mentioned above. By April 1992 the average rate of decrease was the same for each colour (see Table 10.2). This was in contrast to the first nine months of the mission where the rate of decrease had been more significant for the blue spectral region than for the others. The photometry losses were attributed to the decrease in optical transmittance of the associated relay lens system caused by irradiation effects.

10.5. Payload Modelling

As part of the normal data processing, a full geometric calibration was made of the parameters relating the sky coordinates to coordinates on the focal surface. This field-to-grid transformation was derived in the great-circle reductions described in Volume 3, Chapter 9. The development of the transformation parameters, as determined by the FAST and NDAC consortia, are described in Volume 3, Chapter 10.

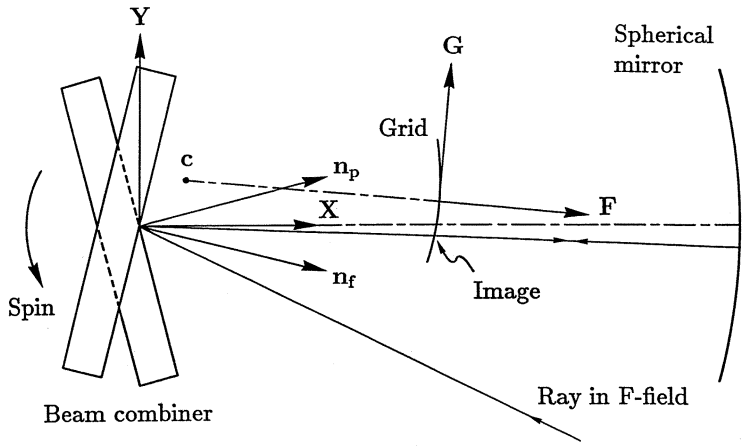

Figure 10.11. *Layout of the simplified geometrical model.*

As an aid for the interpretation of the transformation parameters a simple geometrical model of Hipparcos was developed (Lindegren *et al.*, 1992). By means of the model, basic geometric relations among the optical elements could be estimated and their temporal behaviour assessed. In particular it was of interest to study to what extent the observed transformation and its temporal variation could be attributed to simple geometrical effects, such as displacements and rotations of the optical elements.

The layout of the model is illustrated in Figure 10.11. The basic assumptions of the model are as follows: (i) all optical surfaces are perfect in shape, but may be displaced or tilted; (ii) only rays passing through the centre of curvature of the spherical mirror are traced; (iii) the aperture of the telescope is thus infinitely small, therefore the two segments of the beam combiner can be considered to be flat; and (iv) the imaging properties of this system are invariant to a parallel shift of the beam combiner surfaces, thus it is possible to position both at the centre of curvature of the spherical mirror.

Coordinate Systems and Transformations

The position and orientation of each element are described in a rectangular coordinate system, called the *laboratory frame*. On the other hand, all observations were made relative to the slits of the modulating grid. Nominally, the grid pattern consisted of a number of straight lines generated by an electron beam. The imaginary coordinate system in which the slits occupy their nominal positions is called the *electronic frame*. The model describes the transformation from laboratory coordinates to electronic coordinates; this is done via the intermediary *grid frame*, physically attached to the grid.

The origin of the laboratory frame [**X Y Z**] is chosen to be at the centre of curvature of the spherical primary mirror. This choice eliminates the need to specify any parameters for that mirror, thanks to the spherical symmetry and the assumed infinitely small aperture at the origin. The directions of the axes are defined by the beam combiner: the **Z** axis coincides with the intersection of the two beam combiner surfaces, **X** is the bisector of the mirror normals $\mathbf{n}_p$ and $\mathbf{n}_f$, which are separated by an angle of $\Gamma/2$. In the laboratory frame, the mirror normals are thus written:

$$\begin{aligned} \mathbf{n}_p &= \mathbf{X}\cos(\Gamma/4) + \mathbf{Y}\sin(\Gamma/4) \\ \mathbf{n}_f &= \mathbf{X}\cos(\Gamma/4) - \mathbf{Y}\sin(\Gamma/4) \end{aligned} \qquad [10.16]$$

The grid frame [**F G H**] is physically attached to the grid, with origin at the nominal centre of the grid and the (G, H) coordinates measured in the plane tangent to the grid at the origin, with the slits of the main grid parallel to the H axis. F is measured positively on the convex side of the grid. The radius of curvature, R, which should strictly be a model parameter, is consider a fixed parameter, since a very large change in R would be required to observe a measurable distortion. F can be related to (G, H) by:

$$F = \frac{-(G^2 + H^2)}{R + \sqrt{R^2 - (G^2 + H^2)}} \equiv F(G, H) \qquad [10.17]$$

The relation between the grid frame and the laboratory frame is given by six parameters specifying the displacement and rotation bringing a coordinate triad aligned with [**X Y Z**] into coincidence with [**F G H**]. To effect this realignment the following steps are applied: (1) displace the origin to (X_0, Y_0, Z_0); (2) rotate an angle ψ about the third axis; (3) rotate an angle θ about the second axis; (4) rotate an angle ϕ about the first axis. The resulting transformation is:

$$\begin{pmatrix} X \\ Y \\ Z \end{pmatrix} = \begin{pmatrix} X_0 \\ Y_0 \\ Z_0 \end{pmatrix} + \mathbf{A} \begin{pmatrix} F \\ G \\ H \end{pmatrix} \qquad [10.18a]$$

where:

$$\mathbf{A} = \begin{pmatrix} \cos\theta\cos\psi & \sin\phi\sin\theta\cos\psi - \cos\phi\sin\psi & \cos\phi\sin\theta\cos\psi + \sin\phi\sin\psi \\ \cos\theta\sin\psi & \sin\phi\sin\theta\sin\psi + \cos\phi\cos\psi & \cos\phi\sin\theta\sin\psi - \sin\phi\cos\psi \\ -\sin\theta & \sin\phi\cos\theta & \cos\phi\cos\theta \end{pmatrix} \qquad [10.18b]$$

Ideally, the slit centres should be straight and equidistant lines in the (G, H) plane. However, due to imperfections in the electron beam pattern generator used to produce the grid, they are not. It is therefore necessary to convert from electronic coordinates (g, h) (in which the slits occupy their nominal positions) to the geometrical coordinates (G, H). The transformation from (g, h) to (G, H) includes, in the real instrument, at least the small and medium-scale irregularities of the grid pattern. However, in the present idealised model, only the large-scale distortion caused by a tilting of the electronic frame [**f g h**] with respect to the grid frame is considered. This may be described by two successive rotations: (1) by the angle α about the third axis, and (2) by the angle β about the second axis, which brings [**F G H**] into coincidence with [**f g h**]. This gives the transformation:

$$\begin{pmatrix} F \\ G \\ H \end{pmatrix} = \begin{pmatrix} \cos\beta\cos\alpha & -\sin\alpha & \sin\beta\cos\alpha \\ \cos\beta\sin\alpha & \cos\alpha & \sin\beta\sin\alpha \\ -\sin\beta & 0 & \cos\beta \end{pmatrix} \begin{pmatrix} f \\ g \\ h \end{pmatrix} \qquad [10.19]$$

Calculating (G, H) from (g, h) may be achieved by iterating the equations:

$$\begin{aligned} G &= g\sec\alpha + F\tan\alpha \\ H &= h\sec\beta - F\sec\alpha\tan\beta - g\tan\alpha\tan\beta \\ F &= F(G, H) \end{aligned} \qquad [10.20]$$

starting from $F = 0$. The inverse conversion is obtained from Equation 10.17 and the inverse of Equation 10.19.

Model Parameters

The instrument model, in this simple approximation, can be parameterised by Γ, R, X_0, Y_0, Z_0, ϕ, θ, ψ, α, and β. This can be further simplified, since some of these parameters are redundant. The radius of curvature of the grid, R, is fixed. Y_0 and ψ are coupled since displacing the grid along the **Y** axis is equivalent to a simultaneous rotation of the grid and beam combiner about their respective **Z** axes, plus some second order adjustment of the distance between the two elements. Since a rotation of the beam combiner about **Z** does not change the field-to-grid transformation, Y_0 and ψ are in effect indistinguishable, and thus $\psi = 0$ is chosen. β does not enter the expression for g as a function of (F, G, H) and therefore cannot be determined from the observed distortion of the main field, thus $\beta = 0$ must be assumed. The remaining parameters (Γ, X_0, Y_0, Z_0, ϕ, θ, α) can be freely adjusted to represent the observed field-to-grid transformation as closely as possible.

Relation to the Instrument Frame

The laboratory frame is not directly accessible to observation. Rather, the great-circle reductions establish the relation between the (observable) electronic coordinates and an ideal system of angular coordinates in the two fields of view, the so-called *instrument frame*. In order to interpret the field-to-grid transformation in terms of the model parameters, it is therefore necessary to derive also the relation between the laboratory and the instrument frames.

Given the model, specified by the parameters listed above, the field-to-grid transformation is obtained by tracing a number of rays from different directions in either field of view through the origin $X = Y = Z = 0$ and up to its intersection with the grid surface. If **u** is the unit vector towards a star, the direction of the ray after reflection in the beam combiner is given by:

$$\mathbf{v} = 2\mathbf{n}\mathbf{n}'\mathbf{u} - \mathbf{u} \qquad [10.21]$$

where **n** is the mirror normal from Equation 10.16. After reflection in the spherical mirror, the ray returns to the origin in direction $-\mathbf{v}$. The ray's interception with the grid is computed from the parametric equation $|\mathbf{v}t - \mathbf{c}| = R$. **c**, the position of the centre of curvature of the grid, is obtained by setting $F = -R$ and $G = H = 0$ in Equation 10.18. Solving for t gives:

$$t = \mathbf{v}'\mathbf{c} + \sqrt{R^2 + (\mathbf{v}'\mathbf{c})^2 - \mathbf{c}'\mathbf{c}} \qquad [10.22]$$

The point of interception is $\mathbf{v}t$ in the laboratory system, which can be transformed to the grid frame and then to the electronic frame, via Equation 10.18 and Equation 10.19, yielding the (g, h) coordinates of the ray. To trace a ray in the opposite direction, starting in the laboratory frame, involves the application of Equations 10.20, 10.18 and 10.21.

The instrument frame [**x y z**] with associated field coordinates (w, z) are defined by the optics together with a reference value γ_0 of the basic angle and two features of the grid: (1) the chevron apex of the active star mapper, which defines the origin of the transverse field coordinate z; (2) the centre line of the main field, halfway between the 1344th and 1345th slits, which defines the origin of the longitudinal coordinate w.

The star mapper apex, in electronic coordinates, is $(g_A, 0)$ with $g_A = -21.63385$ mm; the centre line of the main grid is defined by $g = 0$. In the instrument system the two directions in space corresponding to the field point (w, z) are:

$$\mathbf{u} = [\,\mathbf{x}\ \mathbf{y}\ \mathbf{z}\,] \begin{pmatrix} \mp w \sin(\gamma_0/2) + \sqrt{1 - w^2 - z^2}\cos(\gamma_0/2) \\ +w \cos(\gamma_0/2) \pm \sqrt{1 - w^2 - z^2}\sin(\gamma_0/2) \\ z \end{pmatrix} \qquad [10.23]$$

where the upper/lower sign refers to the preceding/following field.

To calculate $[\,\mathbf{x}\ \mathbf{y}\ \mathbf{z}\,]$ in the laboratory system, the following procedure is adopted. A ray from $(g_A, 0)$ is traced through the preceding field. Let $\mathbf{a}_p$ be the resulting unit vector towards the point on the sky that is imaged on the star mapper apex. Similarly the corresponding direction $\mathbf{a}_f$ through the following field is traced. Then:

$$\mathbf{z} = \langle\, \mathbf{a}_f \times \mathbf{a}_p \,\rangle \qquad [10.24]$$

with $\langle\rangle$ denoting vector normalisation. Next we must find the two viewing directions $\mathbf{0}_p$ and $\mathbf{0}_f$, perpendicular to $\mathbf{z}$, which are imaged onto the main field centre line, $g = 0$. This may be done by writing $\mathbf{0}_p = \langle\, \mathbf{a}_p + \mathbf{z} \times \mathbf{a}_p s \,\rangle$ where s is a scalar to be found by solving the equation $g(\mathbf{0}_p) = 0$. The following viewing direction is similarly found by solving s in $\mathbf{0}_f = \langle\, \mathbf{a}_f + \mathbf{z} \times \mathbf{a}_f s \,\rangle$. The remaining instrument axes are then obtained as:

$$\begin{aligned} \mathbf{x} &= \langle\, \mathbf{0}_p + \mathbf{0}_f \,\rangle \\ \mathbf{y} &= \mathbf{z} \times \mathbf{x} \end{aligned} \qquad [10.25]$$

The basic angle is $\gamma = \arccos(\mathbf{0}_p' \mathbf{0}_f)$.

Model Fitting

Stellar observations on the main grid provide a determination of the longitudinal electronic coordinate g as a function of time. The basic assumption is that g increments by exactly 8.2 μm for each light modulation period. The observations are combined in the great-circle reductions to establish an empirical relation between g and (w, z) which may be expressed in terms of polynomial coefficients g_{ij}, h_{ij} in the simplified field-to-grid transformation formula:

$$g = -F_0 w + \sum_{i,j} (g_{ij} \pm h_{ij})\, w^i z^j \qquad [10.26]$$

where F_0 is the reference value for the equivalent focal length. Terms up to 4th order $(i + j < 4)$ were included. The lowest-order terms have a simple physical interpretation: by convention $g_{00} = 0$, which defines the origin of the w coordinate; g_{10} represents a correction to the scale value corresponding to F_0, while g_{01} represents a rotation about the optical axis of the (w, z) frame with respect to the grid. Among the differential terms, h_{00} represents half the correction to the reference basic angle γ_0, h_{10} represents half the difference in scale between the preceding and following fields, and h_{01} represents half the differential rotation of the (w, z) frame.

Given the coefficients g_{ij}, h_{ij} in Equation 10.26 and the corresponding reference values γ_0, F_0, the observed electronic coordinate g_O is obtained for an arbitrary position (w, z) in either field of view. From the geometrical model the 'calculated' coordinate g_C is obtained from Equation 10.23 and a tracing from $\mathbf{u}$ to the electronic frame. g_C depends

on the model parameters which are now adjusted to minimise the mean square deviation in both fields of view:

$$\mathrm{RMS}^2 = \frac{1}{2n^2} \sum_{\mathrm{FOVs}} \sum_{k=1}^{n} \sum_{l=1}^{n} [g_{\mathrm{O}}(w_k, z_l) - g_{\mathrm{C}}(w_k, z_l)]^2 \qquad [10.27]$$

Analysis of the coefficients was done with 98 rays (n = 7) with a digitisation step of 0.0022 in w and z.

The model was applied separately to the field-to-grid transformation data obtained by the NDAC and FAST consortia in their final iterations of the great-circle reductions. Since the consortia used slightly different representations of this transformation the NDAC version, defined by Equation 10.26, was chosen as a common convention for the purpose of this analysis. Converting the FAST results to the NDAC conventions involved a reversal of the axis directions, change of units, and the addition of the nominal transformation. In general a separate great-circle reduction was made for each 'orbit' of science data, i.e. for the (usually) several hours of data collected around each apogee passage in the $\simeq$ 10.7 hour period orbit. Consequently one independent determination of the model parameters Γ, X_0, Y_0, Z_0, ϕ, θ, and α could usually be made for each orbit during the periods when 'good' data were acquired. The results are plotted in Figures 10.12 and 10.13, with NDAC and FAST results on opposite pages. Tables 10.3–6 give examples of the pattern of residuals for the NDAC data at selected points of the mission.

Results

Comparison of the NDAC and FAST results in Figures 10.12–13 shows a remarkably good agreement in some of the parameters (Γ, X_0, Z_0), while systematic shifts are seen in other parameters; in all cases the evolution of the parameters is very similar in the two reductions. There is a striking difference in the amount of scatter, with the FAST results appearing to be significantly more precise. To some extent this reflects a true difference in precision: the FAST great-circle reductions are generally more precise than the NDAC ones, mainly due to the use of both signal harmonics in the FAST analysis (see below). However, the main difference in scatter seen in the diagrams is probably caused by the cubic terms of the field-to-grid transformation, which in NDAC were estimated independently for each great-circle reduction, while in FAST they were kept at constant values for certain time intervals (see Volume 3, Chapter 10).

The systematic shifts of some model parameters between NDAC and FAST may be caused by differences in the reduction procedures that are known to influence the determination of the field-to-grid transformations, such as:

- the FAST reductions used a weighted mean for the first and second harmonics of the main detector signal, whereas only the phase of the fundamental harmonic was used in NDAC data. The phase difference between the two harmonics is of the order of 10 – 20 milliarcsec and variable across both fields of view and with time;
- the observed phases were corrected for medium-scale irregularities of the grid, before they were used to determine the field-to-grid transformation parameters. The medium-scale irregularities were determined from the residuals of the provisional great-circle reductions, and may contain distortion components which are not orthogonal to the present model parameters;

- the determination of some parameters is sensitive to the adopted origin of the field coordinates (w, z), which depends on the assumed geometry of the star mapper grid and on details of the attitude determination, all of which differed somewhat between FAST and NDAC.

While the actual values of the model parameters must consequently be interpreted with some caution, their general evolution in time most likely represents a real physical development of the instrument.

Discussion

The evolution of all model parameters except X_0 are generally rather smooth up to day $\simeq$ 1270. However, there are a few significant jumps especially in Γ and Z_0, e.g. around day 450, 780, 820 and 1000. Some of them can be related to incidents in the thermal control system of the satellite. The evolution of X_0 is characterised by the sudden changes effected by refocusing operations, usually by +2 steps or 2.76 μm. Since X_0 is actually the optical distance between the grid and the curvature centre of the spherical mirror, it is concluded that the mechanical structure connecting the spherical mirror and the flat folding mirror was steadily shrinking; this is compensated by the periodic refocusing moving the grid away from the flat mirror. The rate of shrinking was $\simeq 1.3 \times 10^{-7}$ day^{-1} at the beginning of the mission and $\simeq 1.6 \times 10^{-8}$ day^{-1} two years later.

At the times of optimum focus, which presumably occurred half-way between successive refocusing events, the parameter X_0 equals the effective focal length of the telescope (the measuring-rod being the mean grid step of 8.2 μm). This quantity shows relatively small changes up to day $\simeq$ 1200, the total amplitude being less than 5 μm for most of the mission. This contradicts the tentative conclusion in Section 10.3 that there may be a secular drift of the focal length, by $\simeq$ 10 μm/yr, caused by irradiation of the spherical mirror.

The parameter α is constant to within the measurement errors which is to be expected if this particular distortion pattern was generated during the manufacturing of the grid. The offset in mean value between FAST and NDAC appears to be related to the adopted origin of the z coordinate.

The long-term drifts in X_0, Y_0 and Z_0 are all of the order of 0.1 μm day^{-1}. Also the mean drift in θ, when converted to a linear rate at a distance of 50–100 mm (the size of the grid assembly) is of similar size, while it is 30 times less in ϕ. The typical drift in Γ corresponds to only 10^{-5} μm day^{-1} at the edges of the beam combiner. With the exception of Γ the general tendency is for the drift rates to decrease with time, up to the anomalous behaviour from day 1270. From X_0, ϕ and θ a time constant of approximately one year can be inferred. This is roughly consistent with the assumption that the main changes in the supporting structure are caused by moisture release, as discussed in Section 10.3.

Of considerable interest is to see which terms in the field-to-grid transformation may be 'explained' in terms of the present model, i.e. as arising from simple translations and rotations of the optical elements. A closer examination of the residuals shows that the only terms that attain significant values in the model are: h_{00} (related to the basic angle), g_{10} (scale value), g_{01} (grid rotation about the optical axis), h_{01} (grid displacement along the Z axis), and the terms g_{20}, g_{11}, g_{02}, which may account for a tilting of the grid.

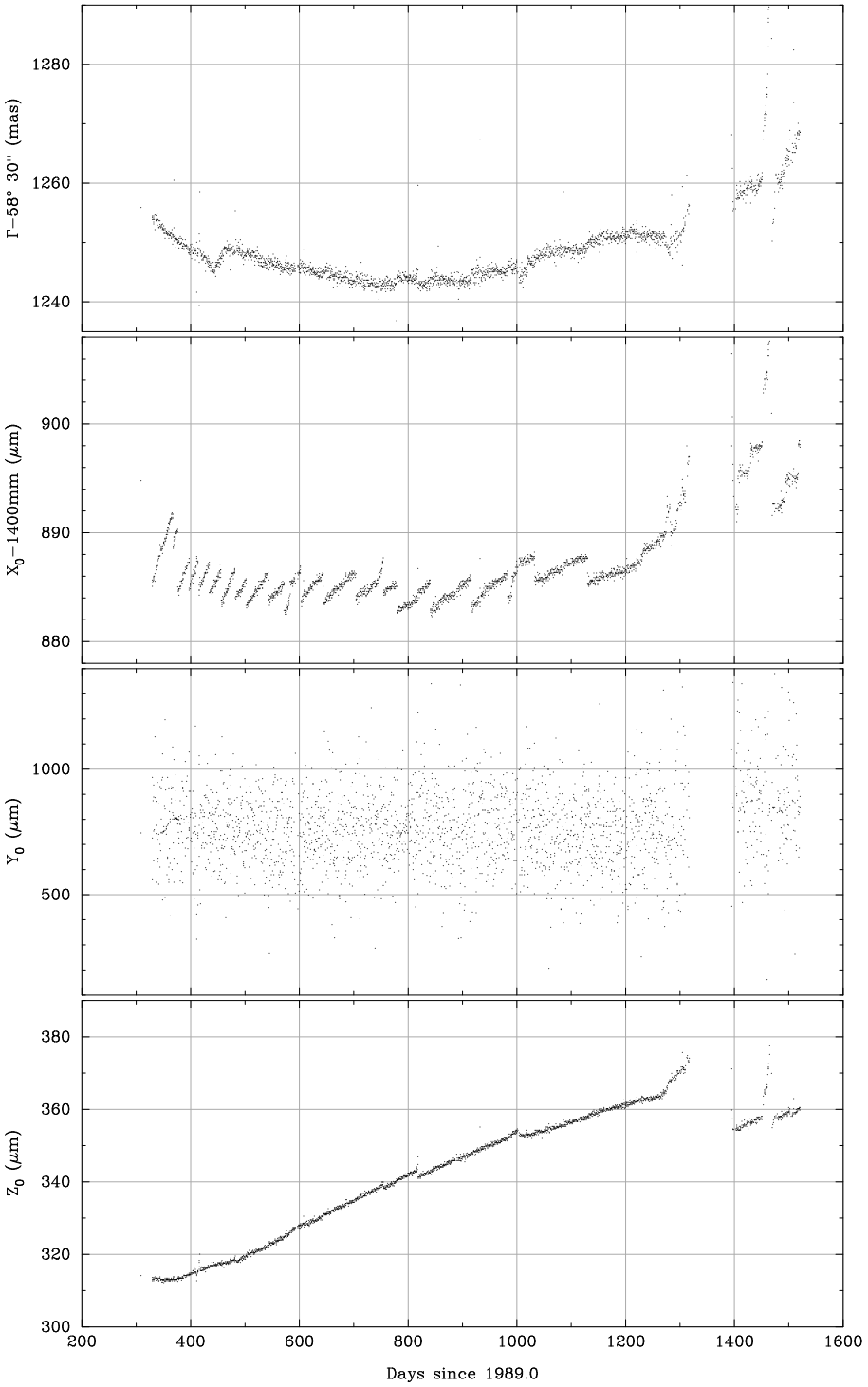

Figure 10.12(a). *Temporal evolution of the model parameters* Γ, X_0, Y_0 *and* Z_0, *using data from NDAC.*

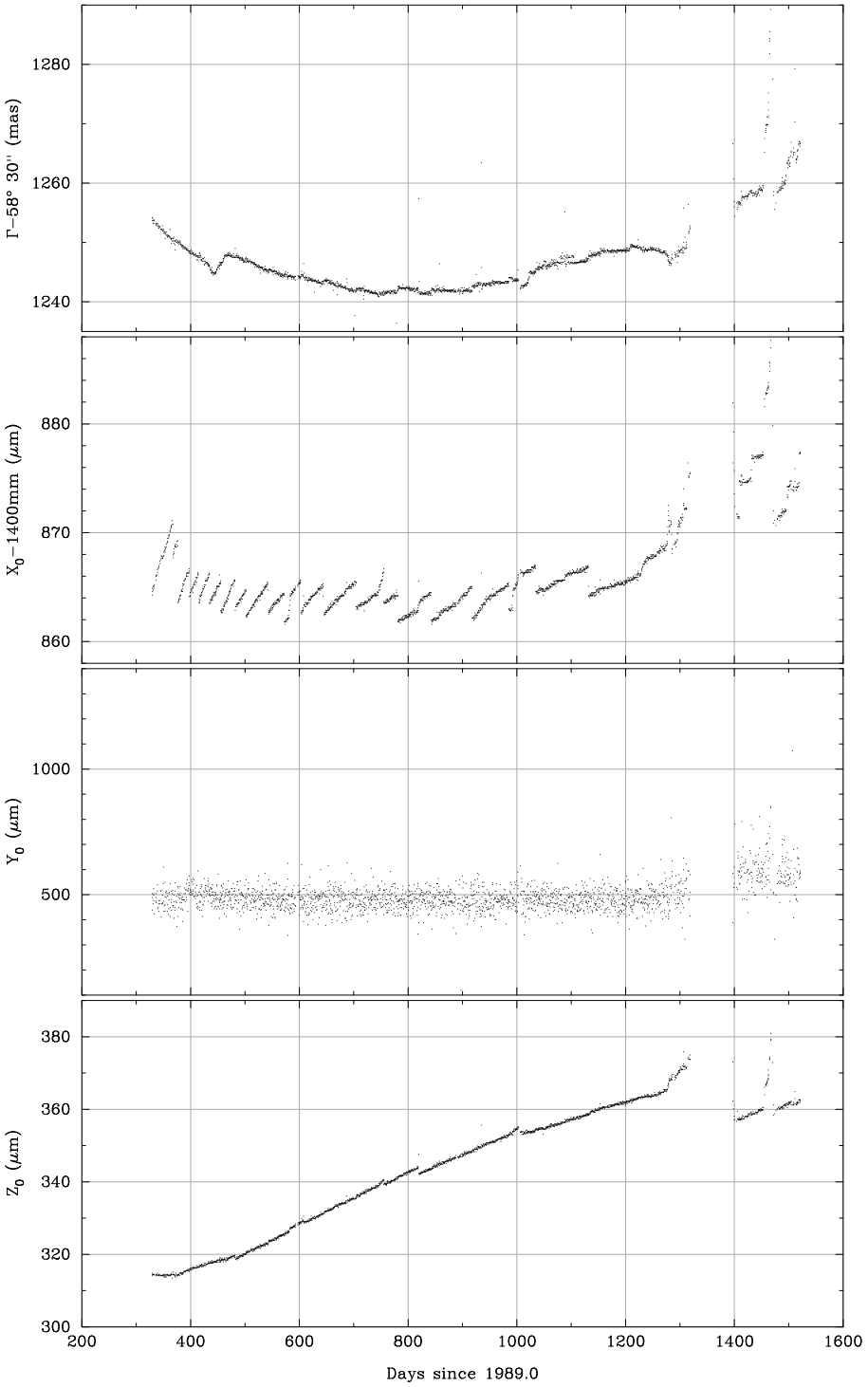

Figure 10.12(b). *Temporal evolution of the model parameters* Γ, X_0, Y_0 *and* Z_0, *using data from FAST.*

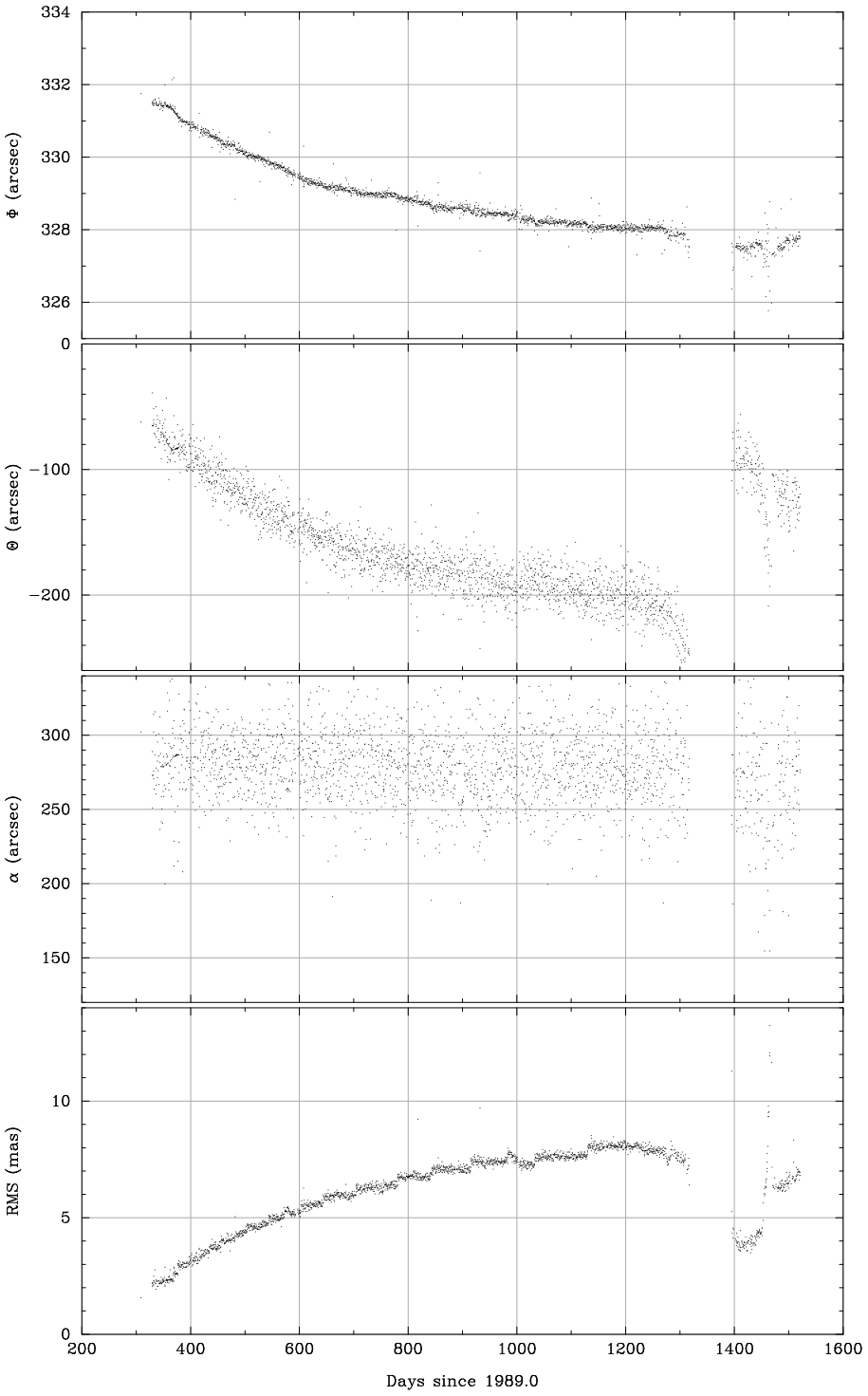

Figure 10.13(a). *Temporal evolution of the model parameters ϕ, θ and α, and of the rms residual of the model fits, using data from NDAC.*

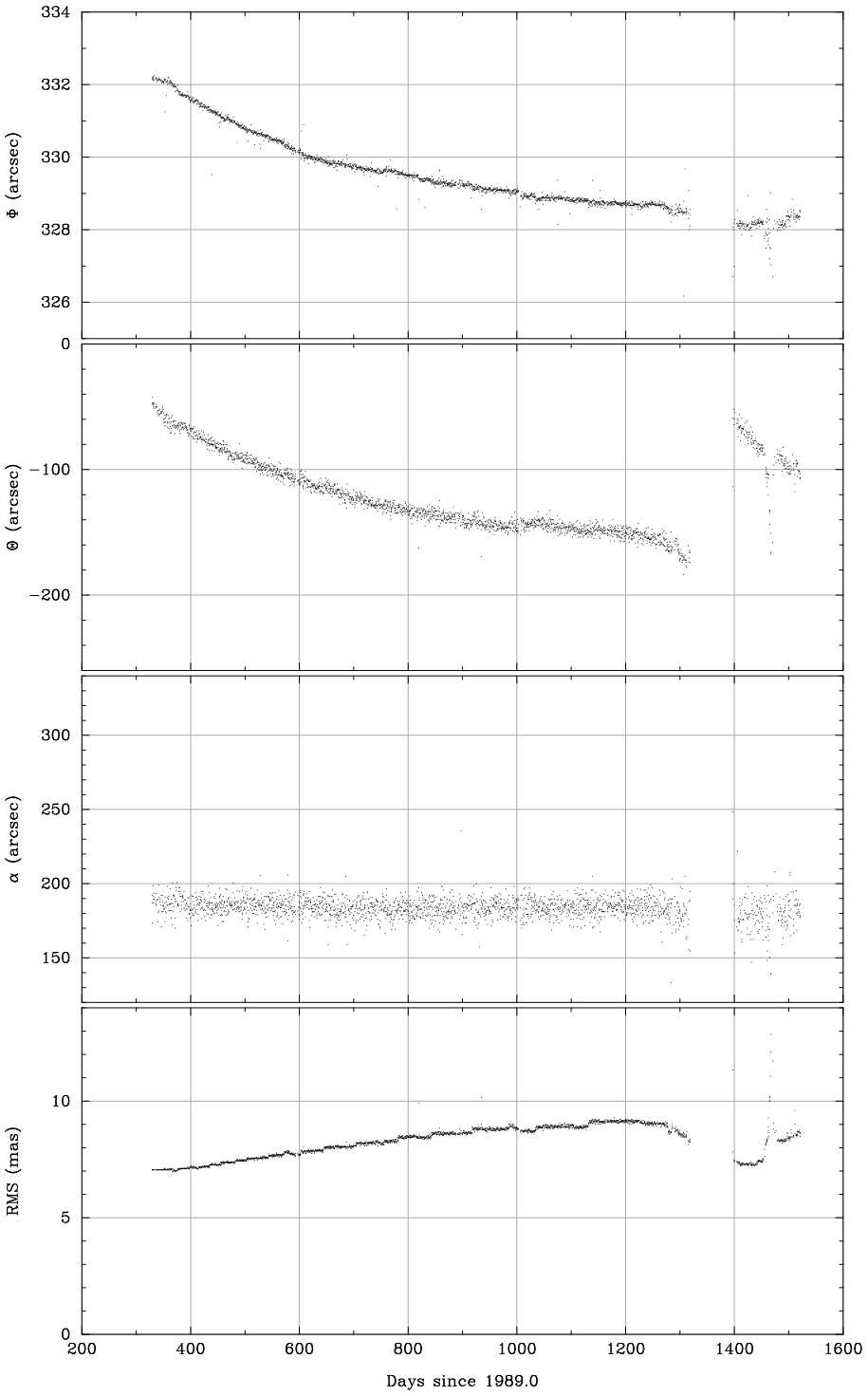

Figure 10.13(b). *Temporal evolution of the model parameters ϕ, θ and α, and of the rms residual of the model fits, using data from FAST.*

Table 10.3. Residuals $g_O - g_C$ (in milliarcsec) versus position in field (w, z) (in milli-rad) from the model fit to the NDAC transformation data for day 309 (5 November 1989, orbit 1).

$z \setminus w$	–6.6	–4.4	–2.2	0.0	2.2	4.4	6.6
Following field of view:							
–6.6	–3.53	–1.47	–0.68	–0.39	0.19	1.84	5.33
–4.4	–1.73	–0.61	–0.69	–1.20	–1.36	–0.37	2.54
–2.2	–0.16	0.26	–0.45	–1.51	–2.15	–1.57	0.99
0.0	1.02	1.00	–0.08	–1.45	–2.32	–1.91	0.57
2.2	1.67	1.46	0.25	–1.17	–2.03	–1.53	1.11
4.4	1.66	1.50	0.41	–0.81	–1.40	–0.57	2.47
6,6	0.83	0.97	0.26	–0.52	–0.60	0.83	4.52
Preceding field of view:							
–6.6	–2.90	0.30	1.71	1.73	0.73	–0.92	–2.83
–4.4	–0.56	1.87	2.70	2.30	1.05	–0.67	–2.47
–2.2	0.46	2.32	2.74	2.12	0.82	–0.78	–2.29
0.0	0.43	1.90	2.12	1.45	0.29	–1.00	–2.03
2.2	–0.40	0.88	1.07	0.56	–0.28	–1.07	–1.42
4.4	–1.76	–0.49	–0.13	–0.30	–0.62	–0.72	–0.21
6.6	–3.39	–1.94	–1.22	–0.86	–0.48	0.30	1.86

Table 10.4. Residuals $g_O - g_C$ (in milliarcsec) versus position in field (w, z) (in milli-rad) from the model fit to the NDAC transformation data for day 1196 (10 April 1992, orbit 2000).

$z \setminus w$	–6.6	–4.4	–2.2	0.0	2.2	4.4	6.6
Following field of view:							
–6.6	–17.77	–10.58	–4.88	–0.07	4.45	9.28	15.00
–4.4	–14.17	–8.41	–4.00	–0.36	3.10	7.00	11.91
–2.2	–11.50	–6.75	–3.23	–0.35	2.47	5.84	10.36
0.0	–9.94	–5.78	–2.74	–0.22	2.38	5.64	10.16
2.2	–9.66	–5.69	–2.71	–0.13	2.64	6.20	11.15
4.4	–10.85	–6.65	–3.33	–0.28	3.08	7.35	13.13
6.6	–13.68	–8.85	–4.77	–0.85	3.51	8.91	15.93
Preceding field of view:							
–6.6	5.11	6.61	5.14	1.72	–2.63	–6.88	–10.02
–4.4	10.45	10.00	6.84	1.99	–3.54	–8.71	–12.51
–2.2	13.20	11.37	7.08	1.36	–4.78	–10.32	–14.23
0.0	13.81	11.15	6.30	0.26	–5.94	–11.28	–14.74
2.2	12.71	9.78	4.91	–0.88	–6.58	–11.16	–13.61
4.4	10.31	7.68	3.36	–1.63	–6.26	–9.53	–10.41
6.6	7.05	5.28	2.07	–1.56	–4.58	–5.97	–4.72

Table 10.5. Residuals $g_O - g_C$ (in milliarcsec) versus position in field (w, z) (in milli-rad) from the model fit to the NDAC transformation data for day 1397 (28 October 1992, orbit 2452).

$z \setminus w$	–6.6	–4.4	–2.2	0.0	2.2	4.4	6.6
Following field of view:							
–6.6	–8.54	–6.22	–4.07	–1.66	1.40	5.54	11.16
–4.4	–6.62	–5.02	–3.60	–1.96	0.32	3.65	8.43
–2.2	–5.21	–3.99	–2.99	–1.78	0.04	2.87	7.14
0.0	–4.53	–3.37	–2.44	–1.35	0.33	3.01	7.08
2.2	–4.79	–3.36	–2.20	–0.89	0.98	3.82	8.03
4.4	–6.22	–4.20	–2.47	–0.62	1.76	5.09	9.77
6.6	–9.04	–6.10	–3.48	–0.77	2.46	6.59	12.06
Preceding field of view:							
–6.6	–0.37	3.29	3.98	2.54	–0.19	–3.33	–6.04
–4.4	4.22	6.20	5.41	2.72	–1.04	–5.01	–8.33
–2.2	6.80	7.55	5.74	2.23	–2.13	–6.48	–9.97
0.0	7.68	7.63	5.23	1.36	–3.15	–7.44	–10.65
2.2	7.14	6.73	4.20	0.40	–3.81	–7.59	–10.08
4.4	5.47	5.15	2.93	–0.35	–3.83	–6.66	–7.98
6.6	2.96	3.18	1.71	–0.60	–2.90	–4.33	–4.05

Table 10.6. Residuals $g_O - g_C$ (in milliarcsec) versus position in field (w, z) (in milli-rad) from the model fit to the NDAC transformation data for day 1466 (4 January 1993, orbit 2607).

$z \setminus w$	–6.6	–4.4	–2.2	0.0	2.2	4.4	6.6
Following field of view:							
–6.6	–23.42	–15.65	–8.90	–2.65	3.60	10.35	18.13
–4.4	–18.75	–11.80	–5.84	–0.37	5.11	11.11	18.15
–2.2	–16.18	–9.74	–4.29	0.69	5.70	11.24	17.82
0.0	–15.39	–9.18	–3.94	0.84	5.66	11.04	17.47
2.2	–16.08	–9.81	–4.49	0.38	5.32	10.81	17.38
4.4	–17.95	–11.32	–5.63	–0.37	4.96	10.87	17.87
6.6	–20.69	–13.41	–7.05	–1.12	4.91	11.52	19.24
Preceding field of view:							
–6.6	9.09	11.41	9.11	3.82	–2.77	–9.03	–13.28
–4.4	14.52	14.17	9.58	2.39	–5.73	–13.13	–18.14
–2.2	17.60	15.30	9.12	0.73	–8.21	–16.04	–21.11
0.0	18.69	15.13	8.07	–0.81	–9.87	–17.43	–21.84
2.2	18.13	14.01	6.78	–1.89	–10.36	–16.95	–20.01
4.4	16.25	12.28	5.58	–2.17	–9.34	–14.25	–15.25
6.6	13.40	10.28	4.83	–1.31	–6.47	–9.00	–7.23

The model cannot reproduce the remaining terms, in particular h_{10} (scale difference between the fields of view) and the cubic terms ($i + j = 3$).

The steadily growing rms residual seen in the bottom panels of Figure 10.12(b) and Figure 10.13(b) is mainly due to the increasing difference in scale between the preceding and following field of view, and to a smaller extent to the cubic coefficients g_{30}, g_{21} and g_{12}. The cubic terms are much more prominent in the FAST residuals than in NDAC, and have a rather significant magnitude already at the beginning of the mission, which explains the higher level of rms residuals in Figure 10.13(b) compared with Figure 10.13(a). In fact, the evolution of the rms residual in Figure 10.13(a) almost exactly mirrors the evolution of the differential scale h_{10} (see Volume 3, Chapter 10), suggesting that this is the main reason for the model mismatch. This is confirmed by a direct inspection of the residuals in Tables 10.3–6.

In contrast to the drifts discussed previously, the evolution of the differential scale and cubic terms, reflected in the increasing rms residuals, can only be understood in terms of deformations of one or several of the mirror surfaces. The scale difference between the preceding and following field of view must be caused by a difference in (mean) curvature between the two halves of one or more of the mirrors (beam combiner, flat folding mirror, or spherical primary mirror).

The differential scale (and consequently the rms residual) was significantly reduced from day 1397, immediately after the period of suspended operations (day 1315 to 1396), until day $\simeq$ 1450. This interval of reduced differential scale (1992.82 to 1992.97) coincides with the period of low ($\simeq -10\,^{\circ}$C) payload temperature shown in Figure 12.4. The sharp increase in differential scale thereafter coincides with the operation in sun-pointing mode (day 1453 to 1466), after which the parameters assumed more normal values. This suggests a thermal mechanism for the development of the differential scale, rather than radiation exposure, at least for the changes on a short time scale. Tables 10.3 to 10.6 show the residuals of the NDAC data at some key dates of this evolution:

Table 10.3: day 309 (beginning of mission);

Table 10.4: day 1196 (after gradual build-up of differential scale);

Table 10.5: day 1397 (immediately after suspension period, low payload temperature);

Table 10.6: day 1466 (end of sun-pointing period).

The residuals of the FAST data are not shown. They are similar to the NDAC residuals except that a strong cubic distortion is superposed, partly obscuring the evolution of the differential scale.

To produce a cubic distortion seems to require a 4th-order deformation of a mirror which is not in the plane of the entrance pupil, i.e. of the folding or spherical mirror. The required deformation is of the order of 50 nm peak value. The corresponding rms wavefront error would be of the order of $\lambda/30$, hardly enough to decrease the light modulation by a significant amount.

10.6. Star Mapper Sensitivity during Suspended Operations

During the first period of suspended operations (see Chapters 15–16) the payload was switched off to save power. When starting the two-gyro real-time attitude determination the star mapper process did not function until a minimum payload mean temperature was reached (approximately 5°C).

On 2 October 1992, the spacecraft was spun down from 0.45 rpm to the nominal spin rate, using modified on-board control software which used only the transverse gyros. Nutation damping was performed. No real-time attitude determination initialisation was possible due to the high background noise in the star mapper signal which was not, however, correlated with the actual solar activity.

A re-commissioning of the payload proceeded over the next three weeks to re-calibrate the single-slit response, basic angle, grid rotation, internal star pattern assembly, grid reference marks, transverse offset and focus position. No significant geometric deformations were detected, although the profile of the single-slit response was significantly broadened, accounting for the difficulties in successfully processing the star mapper data on-board and on-ground. At first, it was thought that the best focus position could be at fault and subsequently the focus position was moved ±80 steps from the previous best focus position. No improvement was seen however.

During the period of suspended operations, the payload had been cooled to −40 °C to reduce the load on the surviving payload heaters. There was no technical reason to believe that the cold payload temperature should affect the star mapper signal in this way. Nevertheless, the decision was taken to re-heat the payload on 25 October 1992. Within a few hours, the star mapper response had improved sufficiently to allow ground real-time attitude determination to initialise the on-board real-time attitude determination. The reason for the sensitivity to temperature of the star mapper detectors was never fully understood. While at low temperatures, the calibrations of the image dissector tube did not suggest any such problems.

After the period of suspended operations, the star mapper response improved significantly (see Figure 10.2), and other instrumental parameters also changed significantly (see Volume 3) for reasons presumably related to the thermal environment experienced during suspended operations, but which were not fully understood.